Acta Materialia 228 (2022) 117748

Contents lists available at ScienceDirect

Acta Materialia

journal homepage: www.elsevier.com/locate/actamat

Full length article

Anisotropic toughening of nanotwin bundles in the heterogeneous nanostructured Cu

H.Z. Zhao[a,b,1], Z.S. You[c,1], N.R. Tao[a], L. Lu[a,2,*]

[a] Shenyang National Laboratory for Materials Science, Institute of Metal Research, Chinese Academy of Sciences, Shenyang 110016, China
[b] School of Materials Science and Engineering, University of Science and Technology of China, Shenyang 110016, China
[c] Herbert Gleiter Institute of Nanoscience, Nanjing University of Science and Technology, Nanjing 210094, China

ARTICLE INFO

Article history:
Received 22 September 2021
Revised 9 February 2022
Accepted 9 February 2022
Available online 15 February 2022

Keywords:
Heterogeneous nanostructure
Nanotwins
Anisotropic toughening
Crack deflection
Strength-toughness synergy

ABSTRACT

In the first report *[H.Z. Zhao, Z.S. You, N.R. Tao, L. Lu, Acta Mater. 210 (2021) 116830]*, anisotropic strengthening of nanotwin bundles in the heterogeneous nanostructured (HNS) Cu was investigated from the perspective of deformation compatibility. To further understand their toughening mechanism, the anisotropic fracture behaviors of this HNS Cu with preferentially oriented nanotwins and elongated nanograins are investigated in this paper. Depending on the orientations of the crack planes relative to the nanotwin bundles (or the alignment of elongated nanograins), the HNS Cu shows a distinctly anisotropic fracture behavior. When both the crack plane and crack growth direction are perpendicular to the nanotwin bundles, HNS Cu exhibits the highest fracture toughness (J_{IC}), which is approximately three times higher than that of the case where both crack plane and crack growth direction are parallel to the nanotwin bundles. This orientation-dependent fracture toughness is attributed to the anisotropic toughening of the nanotwin bundles and the crack deflection caused by the elongated nanograins.

1. Introduction

Homogeneous nanotwinned (NT) metals exhibit a remarkable combination of high strength, moderate ductility and work hardening [2–4]. Significant anisotropic plastic deformation has been recognized for metals with preferentially oriented nanotwins [5–7]. Three distinct dislocation modes, i.e., *Hard Mode I* (dislocation pile-up and transmission across twin boundaries (TBs)), *Hard Mode II* (threading dislocation glide in the twin/matrix lamellar channels), and *Soft Mode* (dislocation gliding parallel to TBs) dominate the plastic deformation with normal, parallel and 45° inclined to TBs, respectively [5–7]. The different dislocation modes are characterized by very diverse flow resistance and strain hardening [5].

Recently, we demonstrated that heterogeneous nanostructure with preferentially oriented nanotwin bundles (NTBs) embedded in a nanograin (NG) matrix also exhibits profound orientation-dependent deformation and mechanical behaviors, which caused by anisotropic strengthening effect of the NTBs and by the orientation-dependent deformation compatibility at the interfaces between the NT regions and surrounding NG matrix [1]. Nanotwins could exert a substantial strengthening effect only when the common deformation of the two microstructural components is activated, e.g., under parallel tension; otherwise, the strengthening of nanotwins cannot be fully effective due to the apparent strain incompatibility [1].

The toughening effect of the NTBs in the HNS metals has been investigated by a series of studies [8–13], which reveal that NTBs not only intrinsically enhance plasticity at the crack tip by suppressing strain localization and void nucleation but also act as crack bridges behind the crack front and extrinsically resist fracture by shielding the crack tip. In contrast to the enormous difference in hardness and elastic/plastic deformation for the elements in traditional composites (e.g., unique hard second phase and soft matrix), the damage always starts at the hard/soft interface due to the mismatch between elastic modulus and plastic deformation [14,15]. The hard but deformable NTBs not only accommodate plastic strain and constrain damage nucleation in the NG matrix, but also promote effective strain transfer at the interfaces, thereby inhibiting the interfacial cracking. The toughening effect of NTBs is also distinct from the softer ductile patches in the bimodal structure, which comes at the expense of the high strength of the NG matrix [16]. However, for now, all the previous studies on the toughening of NTBs focused solely on a single orientation (crack plane perpendicular to the TBs and crack growth direction parallel to TBs)

* Corresponding author.
E-mail address: llu@imr.ac.cn (L. Lu).
[1] Contributed equally.
[2] Lei Lu was an Editor of the journal during the review period of the article. To avoid a conflict of interest, Lei Lu was blinded to the record and another editor processed this manuscript.

https://doi.org/10.1016/j.actamat.2022.117748
1359-6454/

[8–13]. Since the anisotropic deformation of NTBs and the strain compatibility between NTBs and NG matrix may also strongly affect the cracking process, it is reasonable to expect that the toughening behavior associated with NTBs in such hybrid structures will also be extremely influenced by the orientation of the NTBs, like that in uniaxial tensions [1].

However, studies on the orientation-dependent toughening of nanotwins in such HNS metals are lacking, partly because it is still difficult to prepare samples that satisfy the standard dimensions for fracture toughness tests at different orientations. In order to optimize the toughening [17,18], there is a great need to evaluate the fracture toughness of HNS metals with NTBs under different cracking orientations, and to analyze the underlying anisotropic toughening mechanisms associated with the orientation of NTBs.

Here in this study, we perform a systematic investigation on the anisotropic fracture behaviors in HNS Cu composed of NTBs and NGs. Fracture tests based on a custom-designed crack opening displacement (COD) gauging system [19] were conducted on specimens with diverse crack planes to quantitatively assess their fracture resistance. Microscopic toughening mechanisms associated with the orientations of NTBs and elongated NGs are revealed by fractographic examinations and crack-tip microstructural characterizations.

2. Experimental details

2.1. Sample preparation

The NHS Cu sample was prepared by a dynamic plastic deformation (DPD) technique [20,21] at liquid nitrogen temperature with a total accumulative strain (ε) of ~1.5. The detailed processing procedures have been described in Ref. [1]. This bulk sample has a sufficiently large three-dimensional (3-D) size with a thickness of ~14 mm and a diameter of ~45 mm, thus the fracture toughness tests can be conducted under different orientations.

2.2. Fracture toughness tests

The fracture tests were conducted using miniaturized compact tension (CT) specimens with a width, W, of 8 mm, a thickness, B, of 4 mm and an initial notch depth of ~3.2 mm, which are proportionally scaled down from those in the ASTM E1820 standard [22]. To produce sharp crack tips, the specimens were further fatigue pre-cracked under a cyclic tension-tension manner with a frequency of 30 Hz and a stress ratio of 0.1 in an Instron E3000 electro-dynamic tester. To minimize the plastic deformation at the crack tip during the fatigue pre-cracking, only 60% of P_m was used as the maximum fatigue load, where P_m was calculated as per the ASTM E1820 standard [22]. After pre-cracking, the final total crack length, a_0, fell in the range of $0.45W<a_0<0.55W$. Furthermore, to suppress crack-front tunneling and ensure straight crack fronts during crack extension, grooves with a depth of ~0.4 mm (10%B) were machined after fatigue pre-cracking on both sides of the CT specimens by electrical discharge machining (EDM).

To explore the fracture anisotropy, the CT specimens with four different cracking orientations were extracted from the deformed DPD disc, as illustrated in Fig. 1. These CT specimens were labeled with two-letter codes based on the crack plane orientation and crack growth direction with respect to the TBs inside the NTBs, i.e., parallel (P), normal (N), and 45° inclined (I) to the TBs, respectively. Hereafter, these specimens were referred to as P-P, N-N, I-I and N-P (Note: N-P is the orientation investigated in the previous studies [8–13]), where the first letter designated the orientation of the expected crack plane with respect to the TBs, while the second letter designated the crack propagation direction with respect to the TBs.

The fracture toughness tests were performed on an Instron 5848 machine under displacement control with a crosshead speed of 0.1 mm min^{-1}. The force was recorded by the testing machine while the load-line displacements (LLD) were accurately measured by a custom-designed COD gauging system, as described in detail in Ref. [19]. The fracture resistance was evaluated by determining the variation of the J-integral with crack extension (Δa), i.e., J-integral resistance (J-R) curves, following the single-specimen procedure in the ASTM E1820 standard [22]. The instantaneous crack length was monitored by elastic compliance technique in which the specimen was partially unloaded under displacement control with a rate of -0.1 mm min^{-1}. To guarantee the reproductivity, at least three repeated tests were carried out for each orientation.

2.3. Microstructure and fracture feature characterizations

The microstructure of the as-processed DPD Cu and crack-tip deformation zone were examined by back-scattered electrons (BSE) in an FEI Nova NanoSEM 460 scanning electron microscope (SEM). Transmission Kikuchi diffraction (TKD) with a sufficient resolution for analyzing the microstructure of nanostructured materials was used to measure the crystallographic orientation of as-processed microstructure. The TKD measurement was performed using a Zeiss Supra 55 field emission SEM with a step size of 20 nm. The SEM samples were first mechanically polished and then electrochemically polished in an electrolyte of 25 Vol.% phosphoric acid, 25 Vol.% alcohol and 50 Vol.% deionized water at a constant voltage of 5 V. The electron-transparent foil samples used for TKD observations were prepared by firstly mechanical grinding to about 40 μm and then electro-chemical thinning by twin-jet polishing in the electrolyte of 20 Vol.% nitric acid and 80 Vol.% methyl alcohol at about -30°C. The fracture surfaces were examined by SEM (FEI Nova NanoSEM 450) under secondary-electron mode and their 3-D topography was determined by an Olympus LEXT OLS4100 confocal laser scanning microscope (CLSM).

3. Results

3.1. Microstructure characterization

The SEM-BSE images in Fig. 2a schematically show the 3-D microstructure of DPD Cu along the radial direction (RD), tangential direction (TD) and axial direction (AD) of the DPD disc. Transverse-plane microstructure observations by SEM (Figs. 2(b, c)) and TKD (Fig. 2d) clearly reveal a hybrid microstructure with nanotwins in the form of bundles embedded in a matrix of NGs. Statistical results revealed that the average longitudinal size of NTBs is 86±18 μm while the average transverse size is 29±9 μm, representing 30% of the volume. The smaller NTBs shown in Fig. 2d is the result of limited field of view in an electron-transparent foil sample for TKD, where only the small fragmentations of NTBs that separated from the bigger ones can be imaged (as indicated by the white triangles in Fig. 2c). Most of the TBs are perpendicular to the DPD direction (AD), i.e., parallel to the DPD plane (indicated by the shadow pattern in Fig. 2a). The NGs in matrix (Fig. 2d) exhibit elongated shapes and are also aligned almost parallel to DPD plane. The detailed statistics of microstructure parameters are available in Ref. [1].

Fig. 2e shows the Kernel average misorientation (KAM) map based on the TKD data taken from the NG region (here the threshold is predefined as 3° to exclude the points belonging to adjacent grains or subgrains). Statistical distribution in Fig. 2f shows that the local misorientations in the vicinity of the longitudinal grain boundaries (GBs) of nanograins (average value, θ_{mean}=1.24°) are generally larger than that of the short transverse GBs (θ_{mean}=0.75°).

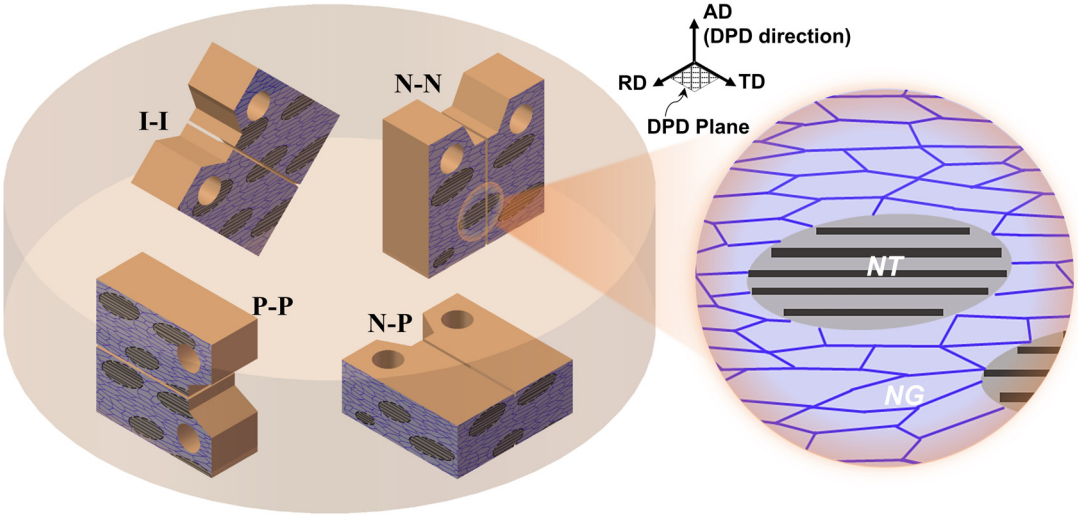

Fig. 1. Schematic illustration of the CT specimens and their orientations in the DPD disc. The microstructural components, i.e., nanotwins (NT) and elongated nanograins (NG) are also schematically illustrated on the cross-sectional plane of each specimen. Additionally, the magnified image on the right side shows the microstructures more clearly (drawing not to scale).

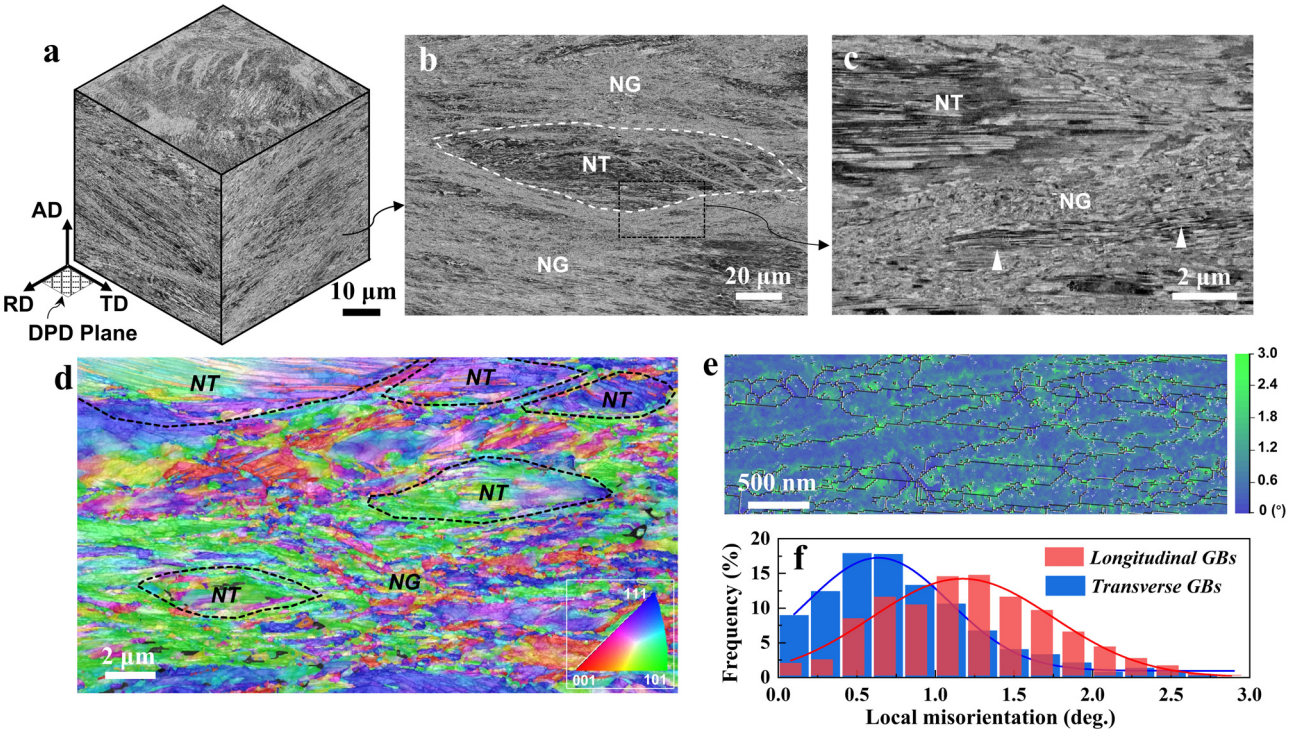

Fig. 2. (a) SEM-BSE images projected on a cube to visualize the microstructure of the DPD Cu in three viewing orientations. (b, c) Typical cross-sectional microstructure, showing nanotwins (NT) in the form of bundles embedded in a matrix of nanograins (NG). (d) Detailed TKD observation on the cross-sectional microstructure, which is plotted as an inverse pole figure (IPF) map with respect to DPD direction (AD). (e) KAM map based on the TKD data taken from the NG region. (f) Statistical distribution of local misorientation angle in the vicinity of the longitudinal and transverse GBs of nanograins, respectively.

3.2. Fracture toughness

Fig. 3a illustrates the force versus LLD curves for different orientations, with partial unloading segments for measuring instantaneous compliances and crack lengths. All curves exhibit significant nonlinearity before reaching peak force, indicating substantial crack tip plasticity prior to crack initiation. In the P-P, the force falls off a cliff, indicating that catastrophic failure shortly after crack initiation; while in the other orientations, the force decreases gradually with increasing LLD, implying steady crack propagation.

The calculated *J*-*R* curves for different orientations are presented in Fig. 3b. According to the ASTM E1820 standard [22], a provisional *J*-integral, J_Q, is defined as the intersection point between the *J*-*R* curve and 0.2 mm offset blunting line (dashed lines in Fig. 3b):

$$J = 2\sigma_Y \Delta a \tag{1}$$

where σ_Y is effective yield strength as the average value of the yield strength (σ_{ys}) and the ultimate tensile strength (σ_{uts}), which are obtained from the tensile tests normal to the corresponding crack planes in Ref. [1] (summarized in Table 1).

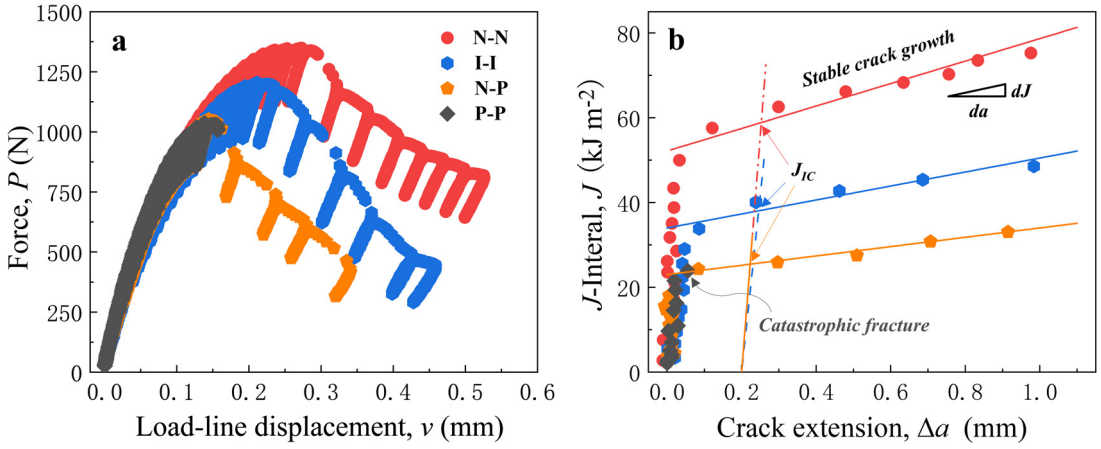

Fig. 3. (a) Force versus load-line displacement curves for the different orientations. The unloading compliance technique is applied to determine the instantaneous crack length. (b) Variation of *J*-integral as a function of crack extension calculated from the data in (a).

Table 1
Tensile properties and fracture toughness of the HNS Cu tested under different orientations.

	σ_{ys} (MPa)	σ_{uts} (MPa)	J_{IC} (kJ m^{-2})	K_{IC} (MPa m$^{1/2}$)	J_i (kJ m^{-2})	K_i (MPa m$^{1/2}$)	T_R
N-N	535 ± 4	580 ± 5	60 ± 2.5	89 ± 1.9	54 ± 7.1	84 ± 5.5	10.3
I-I	367 ± 3	468 ± 6	42 ± 2.1	74 ± 1.8	33 ± 4.3	66 ± 4.3	10.1
N-P	535 ± 4	580 ± 5	27 ± 1.9	60 ± 2.2	25 ± 3.4	57 ± 3.9	4.2
P-P	427 ± 2	483 ± 9	22 ± 2.1	54 ± 1.4	19 ± 1.7	50 ± 2.2	0

σ_{ys}: 0.2% offset yield stress; σ_{uts}: ultimate tensile strength; J_{IC}: critical *J*-integral; K_{IC}: critical stress intensity factor; J_i: local crack initiation *J*-integral evaluated by $CTOD_C$; K_i: stress intensity factor calculated from J_i; T_R: tearing modulus.

For the P-P orientation, catastrophic fracture took place before the crack extension reaches 0.2 mm, here the J_Q value was taken as the *J*-integral at the point of unstable fracture. It is verified that all the specimen dimensions fulfill the *J*-dominant conditions, i.e., $b_0,\ B_N \geq 10J_Q/\sigma_Y$, where $b_0 = W - a_0$ is the initial ligament width and B_N is the net specimen thickness. Therefore, the obtained J_Q values can be qualified as the size-independent plane strain fracture toughness, J_{IC} (summarized in Table 1). Meanwhile, the corresponding critical stress intensity factor, K_{IC}, can be calculated by using the standard *J*-*K* equivalence:

$$K_{IC} = \sqrt{\frac{E\,J_{IC}}{1-\nu^2}} \tag{2}$$

where E=120 GPa is Young's modulus and ν=0.3 is Poisson's ratio for Cu respectively. The calculated K_{IC} for different orientations are listed in Table 1.

In addition, we further estimated the local crack initiation toughness (K_i) by measuring the critical crack opening displacements ($CTOD_C$) at the physical onset of crack extension (Δa=0) on the reconstructed crack profiles (Fig. 4) for comparison with the global fracture toughness in terms of J_{IC} and to verify the differences in fracture resistances for different cracking orientations. These crack profiles were obtained in two steps as follows: 1) typical crack appearances (e.g., transition from a mirror-like fatigue fracture surface to an overload fracture surface with dimples) are first examined by SEM on both sides of the fracture surface at the same location to help to find the exact corresponding points in the CLSM maps, 2) the same areas identified in step 1 are further imaged by CLSM to obtain the 3-D stereo fracture surface topographies (including height information). The combination of SEM and CLSM is capable of providing high enough accuracy to match the corresponding points for $CTOD_C$ evaluation. Then the crack profiles can be extracted from the measured 3-D fracture surface topographies and precisely arranged to the point of coalescence of the first void with the tip of pre-crack. In this manner, the $CTOD_C$ can be established [23]. For each specimen at least nine pairs of crack path profiles at different positions equally spaced along the specimen thickness were conducted to get the average values of $CTOD_C$ and their standard deviations, as indicated in the corresponding crack profiles in Fig. 4.

The local fracture initiation toughness, J_i, can be estimated by using the following relationship [24]:

$$J_i = \frac{1}{d_n}\sigma_Y CTOD_C \tag{3}$$

where the coefficient d_n depends on the hardening exponent (n) and is taken as 0.78 here, which describes the non-hardening behavior [24], and can be considered as a good approximation for present DPD Cu, for its negligible uniform elongation (ε_u) of about 0.6% to 1.0% [1] and limited strain-hardening, n (less than 0.01, considering the numerically equal relationship between n and ε_u [25]). The J_i values calculated by Eq. (3) and the corresponding K_i values are summarized in Table 1. The K_i values are slightly lower than the global K_{IC} values. This is reasonable considering the fact that the crack has extended 0.2 mm and a certain amount of crack growth resistances are involved in the global K_{IC} measurements.

Fig. 3b also demonstrates remarkable variations in the crack growth resistance under different cracking orientations, as reflected by the fairly different slopes of the *J*-*R* curves after crack tip blunting stage. To quantify this, we calculated the nondimensional tearing modulus, T_R, which is defined as [26]:

$$T_R = \frac{E}{\sigma_Y^2}\frac{dJ}{da} \tag{4}$$

where the dJ/da is the slope of the *J*-*R* curves in the stable crack growth regime (as indicated in Fig. 3b). Due to the complete absence of the crack resistance behavior, the T_R value in P-P cannot be obtained and should be a negligible value (≈ 0). The calculated T_R values for the other three orientations are listed in Table 1.

Based on the above measurements, we found that both crack initiation toughness (K_{IC}, K_i) and crack growth resistance (T_R) are

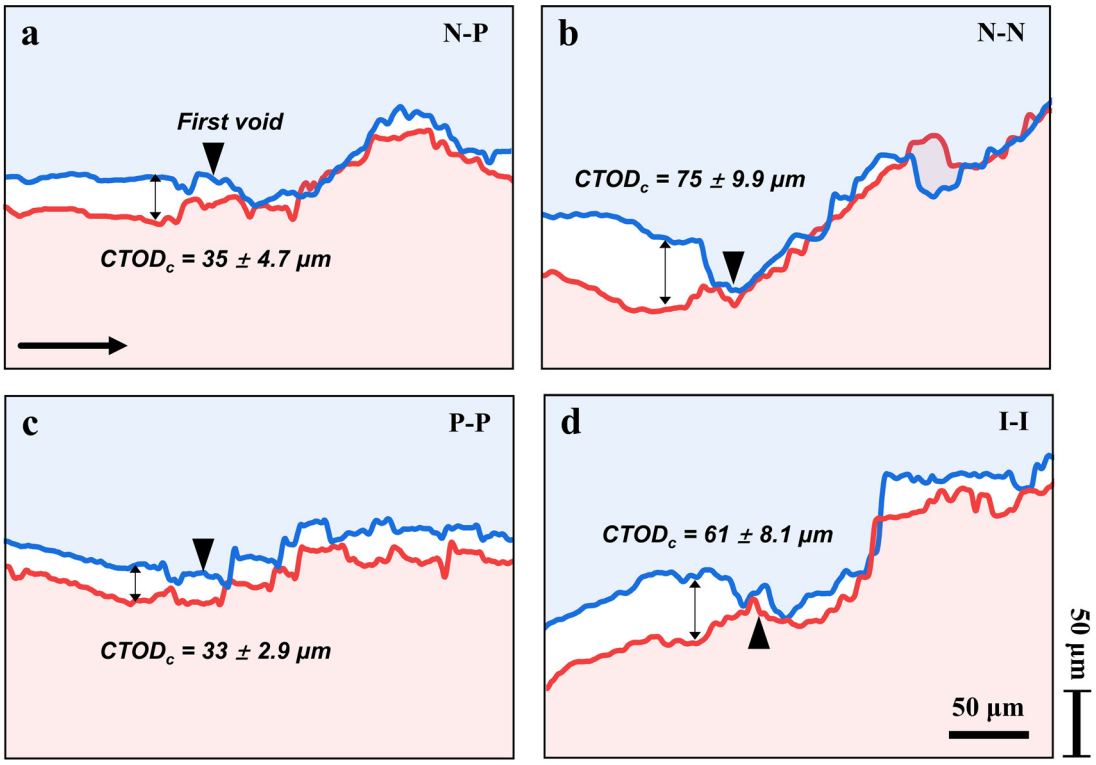

Fig. 4. Profiles of identical crack paths extracted from CLSM 3-D topographies of two fracture halves for N-P (a), N-N (b), P-P (c) and I-I (d) specimens, which are arranged to the points where the first voids (marked by black triangles) prior to coalesces with the blunted pre-crack tips. The black arrows indicate the crack propagation direction, the same as that in the following figures.

significantly orientation-dependent, and these values exhibit an identical variation trend for different orientations. Both N-N and I-I orientations exhibit higher resistances to cracking than the N-P orientation reported in the literatures [8-10,13]. The highest fracture resistance (K_{IC}=89±1.9 MPa m$^{1/2}$, T_R=10.3) was observed in the N-N orientation; while the lowest crack initiation toughness (K_{IC}=54±1.4 MPa m$^{1/2}$) and catastrophic failure occurred in the P-P orientation.

3.3. Macro and microscopic fractographic features

To discern the active failure mechanisms, we examined the fracture surfaces and crack-path profiles for different specimens after fracture tests and found that the fracture surface changes significantly in their morphologies at both macroscopic (Fig. 5) and microscopic scale (Fig. 6).

First, at macroscopic scale, the fracture surface is fairly flat and uniform in N-P (Fig. 5(a1)), while it becomes slightly rougher with some steep steps and ledges in P-P (Fig. 5(b1)). By contrast, fracture surfaces are obviously rugged with serrated peaks and valleys when the crack advances in I-I (Fig. 5(c1)) and N-N (Fig. 5(d1)). The reconstructed crack profiles extracted from the corresponding 3-D fracture surface topographies show predominantly Mode-I crack propagation in both N-P and P-P (Figs. 5(a2, b2)), although in P-P the crack paths are somewhat step-like (Fig. 5(b2)), which is caused by cracks forming at different heights and interconnected by steep cliffs [27,28]. In contrast, the crack paths deviate significantly from Mode I, showing a zig-zag pattern in both I-I and N-N (Figs. 5(c2, d2)), suggesting a microscopic deflection from the expected main crack plane during crack advancement.

At microscopic scale, all the specimens failed in a ductile mode involving micro-void nucleation and coalescence, evidenced by numerous dimples on the fracture surface (Fig. 6). However, these dimples are fairly heterogeneous and can be easily categorized into three characteristic groups according to their size, i.e., coarse dimples (average longitudinal diameter, d=125±32 μm), medium dimples (d=28±10 μm), and fine dimples (d=2.6±1.4 μm). More importantly, these coarse dimples (outlined by the dashed lines) vary significantly in morphology for different specimens. In N-P and N-N (Figs. 6(a, b)), they are deep, elongated, but exhibit different longitudinal orientations with respect to the crack growth direction (along with crack growth direction in N-P while perpendicular to it in N-N); whereas in the P-P and I-I (Figs. 6(c, d)), the coarse dimples are quite shallow with a flat bottom.

It has been well recognized that the coarse dimples with deep and elongated shapes (Figs. 6(a, b)) come from the pulling of NTBs out of NG matrix during fracture process, which can be regarded as evidence of bridging toughening of NTBs during N-P and N-N crack propagation [12,13]. Here, to further reveal this bridging toughening behavior, we performed 3-D topography and crack profiles analysis on the pairs of coarse/deep dimples on the fracture surface of N-P and N-N by CLSM. As shown in Figs. 7(a-d), the two mating fracture surfaces manifest distinct convex and concave contours, respectively. Reconstructed crack profiles in Figs. 7(e, f) reveal that the coarse dimple regions (outlined by dashed lines in Figs. 7(a-d)) are still contacting even though the surrounding regions have already separated (marked by dashed ellipses in Figs. 7(e, f)), demonstrating that the NTBs in these two orientations can act as uncracked ligaments which bridge the crack, consistent with the experimental observation by Xiong et al. [12].

Distinct from the sharp peaks-valleys shapes in N-P and N-N, the coarse dimples developed into flat plateaus-basins topographies in P-P (Figs. 7(g, i)), while similar but obviously slanted topographies in I-I (Figs. 7(h, j)). The flat bottoms of coarse dimples in both P-P and I-I roughly coincide with the elongation planes of the NTBs inside these specimens. Moreover, as shown in the reconstructed crack profiles for these orientations (Figs. 7(k, l)), distinct

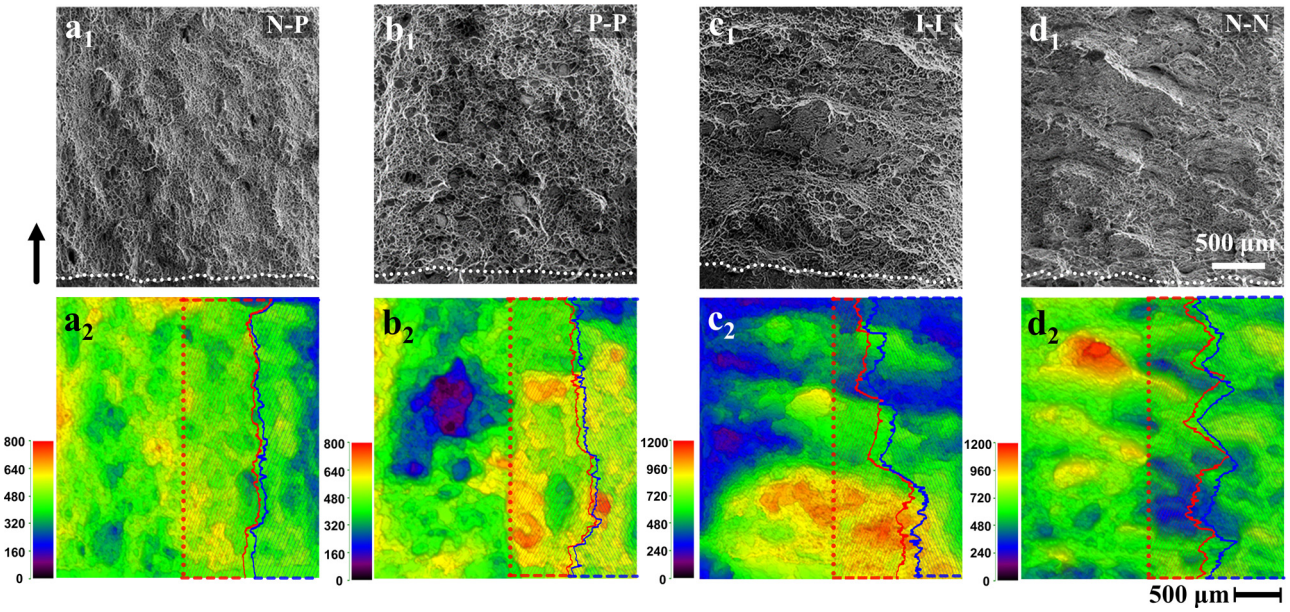

Fig. 5. SEM observations on the macroscopic fractographic features for N-P (a1), P-P (b1), I-I (c1) and N-N (d1). The white dotted lines in (a1-d1) represent the transitions from pre-fatigued regions to overload fracture regions. (a2, b2, c2, d2) Three-dimensional CLSM observations on the area corresponding to (a1, b1, c1, d1), respectively, depicting the height variations of the fracture surface. Colors represent the relative height in the unit of μm. The reconstructed crack profiles (red and blue lines) were extracted along the midlines of each half of the fractured specimens, respectively.

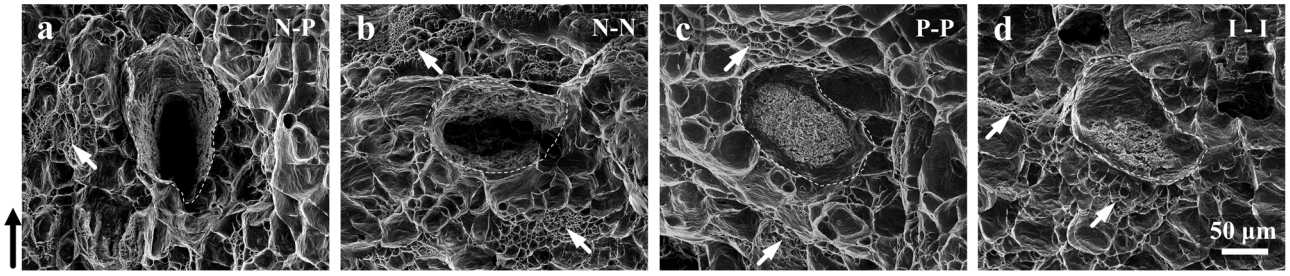

Fig. 6. SEM observations on the microscopic fractographic features for N-P (a), N-N (b), P-P (c) and I-I (d). The coarse dimples (outlined by the white dashed lines) clearly emerged on the uniform background of medium dimples. Additionally, a small number of fine dimples (indicated by white arrows) were also found between the medium ones.

from the coarse/deep dimples in N-P and N-N which are obviously generated during the final fracture due to shear localization, the flat regions (outlined by dash lines in Figs. 7(g-j)) of the coarse dimples in P-P and I-I has been separated already prior to the failure of surrounding areas, reminiscent of micro-cracks nucleate prematurely therein (indicated by the arrows in Figs. 7(k1, l1)). Such micro-cracks have been proven to be initiated at the interfaces between the NTBs and NG matrix, which will be discussed in detail in Section 4.1.

4. Discussion

The above fracture toughness assessments clearly show that HNS Cu embedded with nanotwins exhibits significant anisotropy in both crack initiation (K_{IC}, K_i) and growth toughness (T_R). The remarkable difference in fracture resistance of HNS Cu is related to either the *intrinsic toughening mechanisms* that increase the inherent microstructural resistance to crack initiation or the *extrinsic toughening mechanisms* that shield the crack tip and locally reduce the driving force for crack growth [18]. To reveal the underlying mechanisms responsible for this fracture anisotropy, the anisotropic toughening associated with heterogeneous microstructures is discussed below, particularly for the presence of NTBs as a unique toughening phase and the elongated NGs as matrix.

4.1. Anisotropic toughening of nanotwin bundles associated with deformation compatibility

Plenty of experimental, computational and theoretical studies [29–34] had shown that that the pre-existing nanotwins can intrinsically contribute to the fracture resistance, by accommodating the crack-tip plastic strain and constraining damage nucleation. Regarding intrinsic toughening, unlike homogeneous NG counterpart where cracking proceeds in a brittle-like manner, the pre-existing low-energy twin boundaries are more resistant to void nucleation than the generally high-angle GBs in the NG matrix [29,35], because the built-in stress concentrations in NTBs can be plastically relaxed by different dislocation-TB interactions [36,37]. Therefore, all the initial micro-voids are detected nucleation in the NG matrix, rather than in the NT regions. Furthermore, our preceding work [1] has demonstrated that the inherent plasticity of NTBs plays a critical role in mitigating the interface incompatibility, triggering dense and dispersed shear bands in the NG matrix instead of only one or a few catastrophic shear bands in conventional homogeneous NG materials [38,39], contributing to the delocalization of concentrated strain in NG matrix. This unique constraining effect

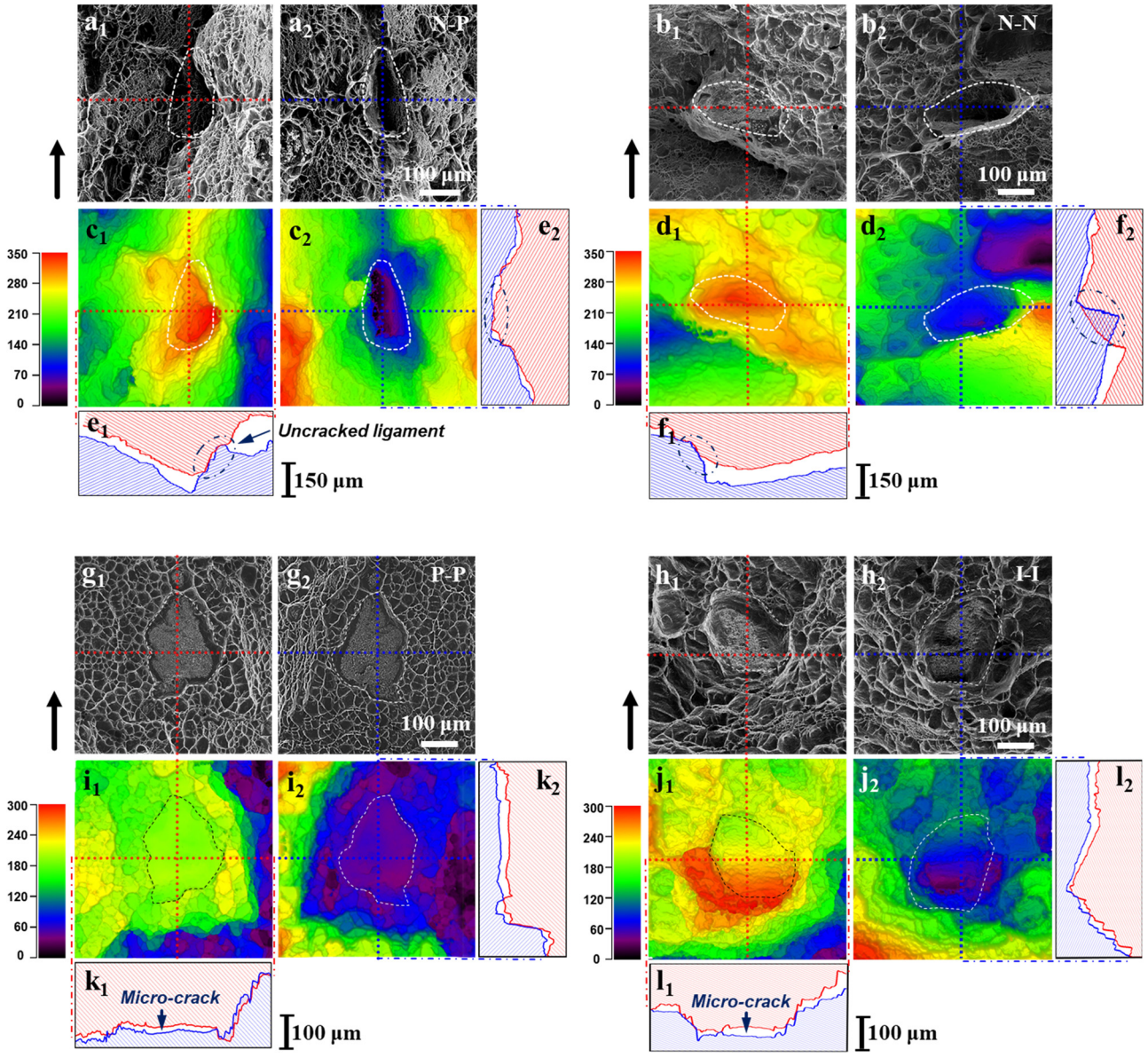

Fig. 7. SEM observations on the pairs of coarse dimples on the fracture surface of two broken halves for N-P (a1, a2), N-N (b1, b2), P-P (g1, g2) and I-I (h1, h2) specimens. (c1, c2, d1, d2, i1, i2, j1, j2) CLSM imaging on the same areas corresponding to (a1, a2, b1, b2, g1, g2, h1, h2), respectively, representing the 3-D morphologies of these dimples. The colors stand for the relative height in the unit of μm. (e1, e2, f1, f2, k1, k2, l1, l2) Horizontal and vertical profiles were extracted from the midsections of the coarse dimples and were meticulously matched together.

effectively delays the nucleation and growth of micro-voids/cracks both in the NG matrix and at the interfaces, as found in the previous studies on an exclusive orientation [12,13,40-44].

However, considering the anisotropic deformation of nanotwins [5–7] and their orientation-dependent deformation compatibility with surrounding NG matrix [1], the accommodation of crack-tip deformation and the damage nucleation in different cracking orientations should be varied. As revealed by the strain field analysis in [1], a compatible co-deformation between NTBs and NG matrix occurred when the tension direction is parallel to TBs, owing to the unique *Hard Mode II* deformation being activated to accommodate the impingement of shear bands initiated in NG matrix. By contrast, neither *Hard Mode I* (when the tension direction is normal to TBs) nor *Soft Mode* (when the tension direction is 45° inclined to TBs) can deform compatibly with the shear banding in NG matrix, making a high heterogeneous strain gradient at the NT/NG interfaces [1].

During the fracture processes, the activated dislocation mechanism in nanotwins, which governs the inherent plasticity of the NTBs as well as their deformation compatibility with NG matrix, should be significantly impact the toughening effect and the fracture anisotropy. As schematically illustrated in Figs. 8(a, b), for N-P and N-N orientations, the deformation of NTBs at the crack tip or at the inter-void ligaments is comparable to the uniaxial tension case parallel to TBs, therefore the same deformation mode of *Hard Mode II* activated in NTBs [45,46]. For these cases, good deformation compatibility would be developed between NTBs and surrounding NG matrix [1], owing to the unique interactions between shear bands and threading dislocation slip (*Hard Mode II*) in nanotwins, which allows the shear bands to be uniformly distributed along the NT/NG interfaces without causing dangerous stress concentrations [1]. As a consequence, the fracture initiation at such interfaces is mitigated and is pushed far away from NTBs into the NG matrix [12,13,40-44].

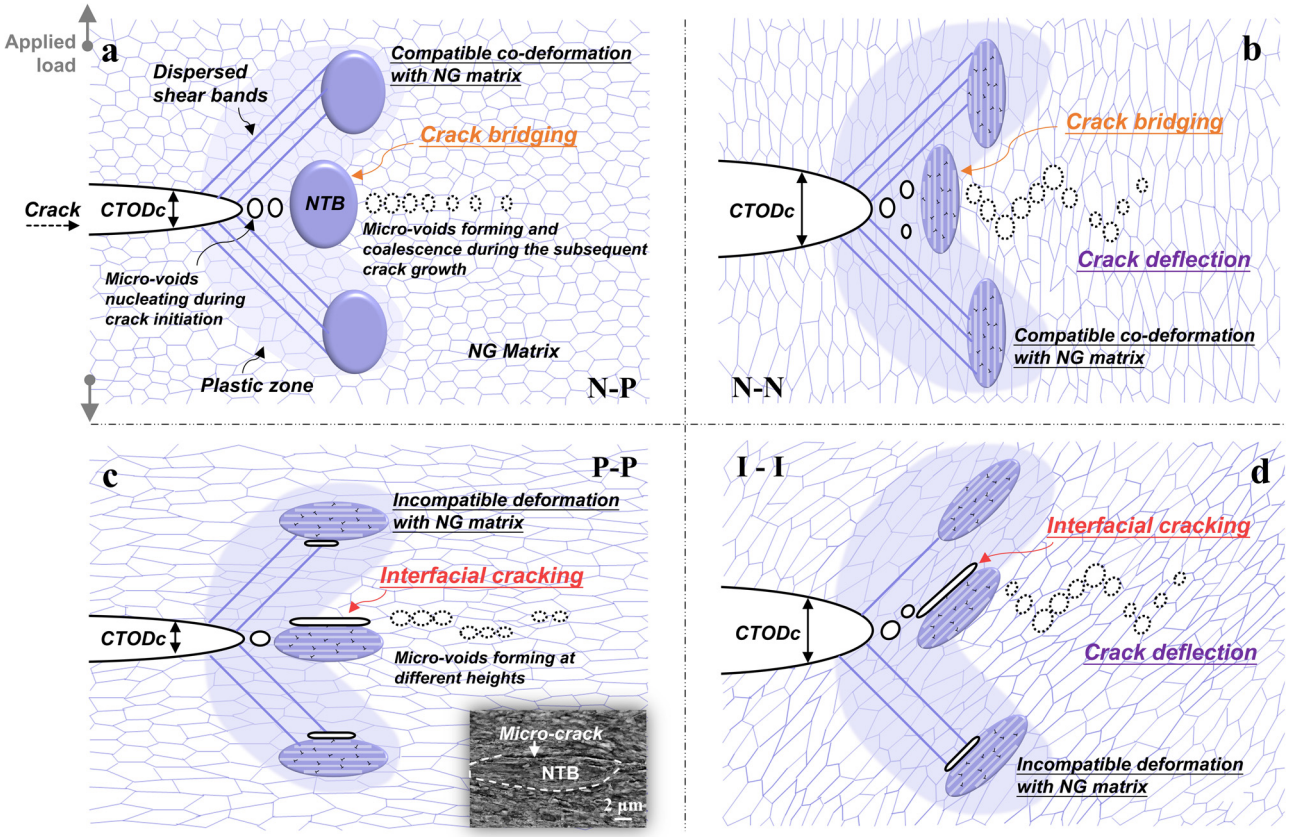

Fig. 8. Schematic illustrating the fracture process in different cracking orientations: (a) N-P, (b) N-N, (c) P-P and (d) I-I. The anisotropic toughening behaviors of NTBs and the crack propagation paths in NG matrix are highlighted (the sizes of nanograins are drawn not to scale). The insert SEM image in (c) shows a micro-crack (indicated by the white arrow) on the crack tip of P-P specimen, which initiated at the longitudinal interface between the NTB (outlined by the white dashed line) and NG matrix.

By contrast, in both the P-P and I-I cases (Figs. 8(c, d)), incompatible deformations occur between the NTBs and surrounding NG matrix (comparable to the uniaxial tension normal and 45° inclined to TBs, respectively [1]), resulting in high heterogeneous strain gradients and thus large tensile traction at the NT/NG interfaces, which causes premature interfacial damage nucleation and reduced crack-tip plasticity [47,48]. This interfacial cracking behavior in P-P and I-I has been proved by the reconstructed crack profiles in Figs. 7(k, l) and was further confirmed by the SEM examinations on the crack tip of the P-P specimen. As shown in the inset of Fig. 8c, flat micro-cracks were indeed detected at the longitudinal NT/NG interfaces before the micro-voids initiation in NG region.

As for the extrinsic toughening, pre-existing NTBs can also affect the microscopic crack paths during crack growth, which are also closely related to the orientation of NTBs and their strain compatibility with surrounding NG matrix. As revealed by the previous studies on N-P orientation [12,13], and is further demonstrated by the crack profiles analysis in Figs. 7(a, c, e) that the NTBs can act as uncracked ligaments, which bridge cracks, carrying load and resisting crack propagation. Here, a similar crack bridging effect is also found in N-N orientation (Figs. 7(b, d, f)), as the longitudinal directions of the NTBs is normal to the crack opening plane in both N-N and N-P. In these orientations, as depicted in Figs. 8(a, b), crack propagation is carried out by preferential micro-voids nucleation and growth in NG matrix, while similar damage generation is completely suppressed both in the NT regions and at the NT/NG interfaces [12,13]. As a consequence, the crack takes a more tortuous path by passing around the NTBs, leaving them as uncracked bridging ligaments in the wake of the main crack to enhance the fracture resistance [12,13]. With the crack further opening, NTBs are eventually extracted by shearing from the NG matrix (Figs. 7(e, f)), resulting in the coarse dimples with deep and elongated shapes on the fracture surface [12]. The small difference between the N-P and N-N is the different longitudinal orientations of coarse/deep dimples (Figs. 6(a, b)). This is because in N-P the crack advances parallel to the twin planes (Fig. 8a), whereas in N-N it advances normal to twin planes (Fig. 8b). The crack growth resistance in N-N is larger than in N-P (see Fig. 3b and Table 1), suggesting that the toughening effect of NTBs is substantially enhanced when the crack runs perpendicular to the TBs (Fig. 8b).

In contrast, the extrinsic toughening related to NTBs behaves rather diversely in P-P and I-I orientations. As shown in Figs. 8(c, d), the micro-cracks are nucleated prematurely along the longitudinal interfaces between the NTBs and the NG matrix before the formation of micro-voids in NG matrix. Such interfacial cracks parallel (P-P) or inclined (I-I) to the macroscopic crack plane and thus developed predominantly under pure Mode I (opening mode) or the mixed mode involving Mode II (sliding mode), as shown in Figs. 7(k2, l2), making the NTBs separate easily from the NG matrix, leading to the shallow/flat fracture facets observed in Figs. 6(c, d)). Consequently, caused by the premature failure of NT/NG interfaces, the crack bridging effect of the NTBs should not be functional in P-P and I-I orientations.

However, though the interfacial cracks developed in I-I (Fig. 8d), which still exhibits marked crack-tip blunting and high resistance to crack growth, as reflected by the larger $CTOD_C$ and T_R (see Fig. 4d and Table 1), this is attributed to the elongated shapes of nanograins and their alignments relative to the crack propagation direction, which will be discussed in detail as follows.

4.2. Crack deflection induced by the elongated nanograins

In addition to the anisotropic toughening of NTBs, the orientation-dependent fracture resistance of the HNS Cu is also intimately associated with the elongated grains in the matrix. Numerous fracture mechanics evaluations on homogeneous nanostructured metals produced by severe plastic deformation (SPD) have quantitatively demonstrated that the preferential alignment and elongation of the refined grains led to a profound anisotropic fracture toughness [27,28,49-52]. It is accepted that the extended GBs with accumulated extrinsic dislocations are favorable nucleation sites for micro-voids during ductile fracture and decisively control fracture anisotropy [27,28,49,53].

Considering the monotonic impact loading during the DPD processing, the NGs in the matrix are elongated as well (Fig. 2d). The KAM analysis in Fig. 2e reveals that the longitudinal GBs that perpendicular to the DPD direction (AD) have higher local misorientations and thus probably contain more extrinsic dislocations preferentially lie on DPD plane (as indicated in Fig. 2a). A corollary of the extended GBs arrangements are susceptible to micro-void nucleation [53–55], and thus the DPD plane is less resistant to fracture and critically mediates the fracture process in the NG matrix. When the crack propagation direction is parallel to the DPD plane, as in P-P and N-P orientations (Figs. 8(a, c)), micro-voids can nucleate and coalesce easily ahead of the crack tip [27,28,49], as evidenced by the reduced $CTOD_C$ (Figs. 4(a, c)). Following these processes, the micro-voids develop into macroscopic crack along the straight Mode I path (Figs. 5(a2, b2)), with less fracture surface raggedness and lower fracture resistances (Fig. 3b).

However, in I-I and N-N, as depicted in Figs. 8(b, d), the main crack tends to deflect microscopically, as the DPD plane is inclined at a large angle to the expected cracking direction. As a result, initiation and growth of micro-voids along the longitudinal GBs become difficult [27,28,49], as reflected by the enhanced $CTOD_C$ (Figs. 4(b, d)). To follow the DPD plane, micro-voids tend to develop along more oblique paths, leading to extremely tortuous and macroscopic zig-zag crack growth paths in the I-I and N-N (Figs. 5(c2, d2)). The enhanced crack deflection contributes significantly to the fracture resistance, and especially to the crack growth toughness (see Table 1). Since the local driving force of a deflected crack tip is less than that of a straight crack under the same far-field stress, a higher global driving force for crack extension is demanded [56,57]; on the other hand, the crack deflection increases the effective crack path and dissipates more irreversible plastic work [58,59]. Therefore, the I-I exhibits higher fracture resistance despite absence of the bridging toughening effect of NTBs.

4.3. Superior strength-toughness synergy

With respect to the damage tolerance of HNS Cu in this study, a comparison with other nanostructured Cu [13,27,28,60] is shown on the Ashby map of fracture initiation toughness versus yield strength (Fig. 9). Since the global fracture initiation toughness (K_{IC}) values in the literatures are likely to be related to specimen size and geometry [19], a comparison is made here using the microscopic fracture initiation toughness (K_i), which is inherently a material parameter and is less affected by specimen size [61]. As shown in Fig. 9, HNS Cu possesses an exceptional combination of high strength and substantial fracture resistance. The high strength is intimately correlated with the presence of NTBs and nanograins [62–64], whereas the enhanced fracture resistance originates different toughening mechanisms related to the heterogeneous structure.

As indicated by the gray dashed arrow in Fig. 9, the introduction of nanotwins in HNS Cu can effectively improve the toughness and yield strength in the comparison of P-P to homogeneous nanostructured Cu (equal channel angular pressing (ECAP) Cu) fractured in a comparable orientation (parallel to grain elongation plane (GEP)) [27,28]. Then, HNS Cu is further toughened solely by crack bridging in N-P [12,13] or by crack deflection in I-I. Crack deflection has also been shown to be the main toughening mechanism for homogeneous nanostructured metals with elongated grains [27,28,49], which appears to be more effective than crack bridging by comparing the fracture toughness values of I-I and N-P. Finally, by further combining all the three toughening mechanisms, i.e., nanotwinning, crack bridging and deflection, N-N oriented HNS Cu achieves a superior combination of fracture toughness (~90 MPa $m^{1/2}$) and yield strength (535 MPa), much better than that reported so far in pure Cu.

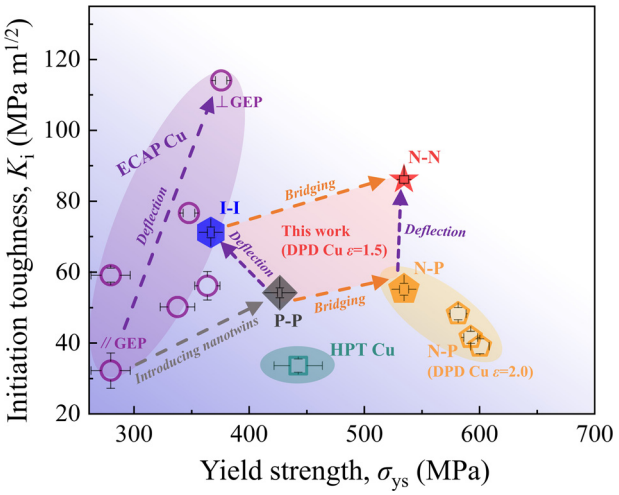

Fig. 9. The relationship between the yield strength (σ_{ys}) and the initial fracture toughness (K_i) for HNS Cu (DPD Cu ε=1.5) under different cracking orientations, i.e., N-N, I-I, N-P and P-P, which are compared with the ECAP Cu [27,28] under different cracking orientations (⊥GEP and ∥GEP indicate the crack planes perpendicular and parallel to the grain elongation plane (GEP), respectively), high pressure torsion (HPT) Cu [60], and DPD Cu (ε=2.0) with different NTB lengths in N-P orientation [13].

It is clear that the damage tolerance of HNS copper is anisotropic, with fracture toughness varying considerably with the direction of fracture. Traditionally, this anisotropy is not expected from an engineering point of view. However, in some applications, high fracture resistance in only one or two fracture directions is required [65]. Therefore, significant fracture anisotropy can be a potential strategy to make high-strength nanostructured materials sufficiently tough and safe in the critical directions [49]. The systematic investigation on the anisotropic fracture behaviors of HNS Cu in this work not only deepens our understanding of the fracture mechanism of heterostructured materials, but also provides a practical guide to extend the safe industrial applications of such materials.

5. Conclusion

The fracture behavior of HNS Cu composed of anisotropic NTBs and elongated nanograins was comprehensively evaluated by elastic-plastic fracture mechanics based on *J*-integral. Depending on the crack orientations relative to the NTBs and the alignments of the elongated nanograins, HNS Cu exhibited significant anisotropy in both the fracture initiation toughness (K_{IC}, K_i) and crack growth toughness (T_R). The apparent fracture anisotropy is related to anisotropic toughening of NTBs and crack deflection caused by elongated nanograins. NTBs provide effective toughening in the N-N and N-P orientations by acting as unbroken bridges to inhibit crack opening; while in the P-P and I-I orientations, bridg-

ing toughening does not work due to the micro-cracks prematurely initiate at the interfaces of NTBs and NG matrix. In addition, apparent crack deflection in N-N and I-I orientations contributes to the higher fracture resistance. The combined high strength and remarkable fracture toughness found in one of the orientations (N-N) where both crack bridging and crack deflection toughening mechanisms are activated, implying the anisotropy can be a potential strategy for toughening high-strength nanostructured material in a critical direction.

Declaration of Competing Interest

The authors declare that they have no known competing financial interests or personal relationships that could have appeared to influence the work reported in this paper.

Acknowledgments

The authors acknowledge financial support by National Science Foundation of China (NSFC, Grant Numbers. 51931010 and 92163202), the Key Research Program of Frontier Science and International partnership program (Grant Number. GJHZ2029), CAS, and LiaoNing Revitalization Talents Program (Grant Number. XLYC1802026). Z.Y. acknowledges financial support by the National Key R&D Program of China (Grant No. 2017YFA0204403).

References

[1] H.Z. Zhao, Z.S. You, N.R. Tao, L. Lu, Anisotropic strengthening of nanotwin bundles in heterogeneous nanostructured Cu: effect of deformation compatibility, Acta Mater. 210 (2021) 116830.
[2] L. Lu, X. Chen, X. Huang, K. Lu, Revealing the maximum strength in nanotwinned copper, Science 323 (2009) 607–610.
[3] L. Lu, Y.F. Shen, X.H. Chen, L.H. Qian, K. Lu, Ultrahigh strength and high electrical conductivity in copper, Science 304 (2004) 422–426.
[4] Y.F. Shen, L. Lu, Q.H. Lu, Z.H. Jin, K. Lu, Tensile properties of copper with nano-scale twins, Scr. Mater. 52 (2005) 989–994.
[5] Z.S. You, X.Y. Li, L.J. Gui, Q.H. Lu, T. Zhu, H.J. Gao, L. Lu, Plastic anisotropy and associated deformation mechanisms in nanotwinned metals, Acta Mater. 61 (2013) 217–227.
[6] T. Zhu, H.J. Gao, Plastic deformation mechanism in nanotwinned metals: an insight from molecular dynamics and mechanistic modeling, Scr. Mater. 66 (2012) 843–848.
[7] Q.H. Lu, Z.S. You, X.X. Huang, N. Hansen, L. Lu, Dependence of dislocation structure on orientation and slip systems in highly oriented nanotwinned Cu, Acta Mater. 127 (2017) 85–97.
[8] E.W. Qin, L. Lu, N.R. Tao, J. Tan, K. Lu, Enhanced fracture toughness and strength in bulk nanocrystalline Cu with nanoscale twin bundles, Acta Mater. 57 (2009) 6215–6225.
[9] E.W. Qin, L. Lu, N.R. Tao, K. Lu, Enhanced fracture toughness of bulk nanocrystalline Cu with embedded nanoscale twins, Scr. Mater. 60 (2009) 539–542.
[10] S.S. Luo, Z.S. You, L. Lu, Intrinsic fracture toughness of bulk nanostructured Cu with nanoscale deformation twins, Scr. Mater. 133 (2017) 1–4.
[11] L. Xiong, Z.S. You, L. Lu, Enhancing fracture toughness of nanotwinned austenitic steel by thermal annealing, Scr. Mater. 119 (2016) 55–59.
[12] L. Xiong, Z.S. You, S.D. Qu, L. Lu, Fracture behavior of heterogeneous nanostructured 316L austenitic stainless steel with nanotwin bundles, Acta Mater. 150 (2018) 130–138.
[13] Z.S. You, S.S. Luo, L. Lu, Size effect of deformation nanotwin bundles on their strengthening and toughening in heterogeneous nanostructured Cu, Sci. China Technol. Sci 64 (2020) 23–31.
[14] Q. Lai, O. Bouaziz, M. Gouné, L. Brassart, M. Verdier, G. Parry, A. Perlade, Y. Bréchet, T. Pardoen, Damage and fracture of dual-phase steels: Influence of martensite volume fraction, Mater. Sci. Eng. A 646 (2015) 322–331.
[15] M.F. Ashby, The deformation of plastically non-homogeneous materials, Philos. Mag. A 21 (1970) 399–424.
[16] B.O. Han, Z. Lee, D. Witkin, S. Nutte, E.J. Lavernia, Deformation behavior of bimodal nanostructured 5083 Al alloys, Metall. Mater. Trans. A 36A (2005) 957–965.
[17] K. Lu, The future of metals, Science 328 (2010) 319–320.
[18] R.O. Ritchie, The conflicts between strength and toughness, Nat. Mater. 10 (2011) 817–822.
[19] Z.S. You, S.D. Qu, S.S. Luo, L. Lu, Fracture toughness evaluation of nanostructured metals via a contactless crack opening displacement gauge, Materialia 7 (2019) 100430.
[20] N.R. Tao, K. Lu, Dynamic plastic deformation (DPD): a novel technique for synthesizing bulk nanostructured metals, J. Mater. Sci. Technol. 23 (2007) 771–774.
[21] Y.S. Li, N.R. Tao, K. Lu, Microstructural evolution and nanostructure formation in copper during dynamic plastic deformation at cryogenic temperatures, Acta Mater. 56 (2008) 230–241.
[22] ASTM E1820-15Standard Test Method for Measurement of Fracture Toughness, American Society of Testing and Materials, Philadelphia PA, 2015.
[23] J. Stampfl, S. Scherer, M. Berchthaler, M. Gruber, O. Kolednik, Determination of the fracture toughness by automatic image processing, Int. J. Fract. 78 (1996) 35–44.
[24] C.F. Shih, Relationships between the J-integral and the crack opening displacement for stationary and extending cracks, J. Mech. Phys. Solid 29 (4) (1981) 305–326.
[25] M.A. Meyers, K.K. Chawla, in: Mechanical Behavior of Materials, second ed., Cambridge university press, New York, 2009, pp. 172–173.
[26] R.O. Ritchie, A.W. Thompson, On macroscopic and microscopic analyses for crack initiation and crack growth toughness in ductile alloys, Metall. Trans. A 16 (1985) 233–248.
[27] S.D. Qu, Z.S. You, R.C. Gu, Y. Jiang, J.T. Wang, Fracture toughness anisotropy of ultrafine-grained pure copper processed by equal channel angular pressing, Mater. Sci. Eng. A 782 (2020) 139260.
[28] S.D. Qu, Z.S. You, R.C Gu, Y. Jiang, J.T. Wang, Regarding fracture plane with minimum toughness and fracture anisotropy associated with elongated grain boundaries in ultra-fine-grained Cu, Eng. Fract. Mech. 247 (2021) 107654.
[29] X.Y. Li, M. Dao, C. Eberl, A.M. Hodge, H.J. Gao, Fracture, fatigue, and creep of nanotwinned metals, MRS Bull. 41 (2016) 298–304.
[30] S.W. Kim, X.Y. Li, H.J. Gao, S. Kumar, In situ observations of crack arrest and bridging by nanoscale twins in copper thin films, Acta Mater. 60 (2012) 2959–2972.
[31] Z. Zeng, X.Y. Li, L. Lu, T. Zhu, Fracture in a thin film of nanotwinned copper, Acta Mater. 98 (2015) 313–317.
[32] Z.W. Shan, L. Lu, A.M. Minor, E.A. Stach, S.X. Mao, The effect of twin plane spacing on the deformation of copper containing a high density of growth twins, JOM 60 (2008) 71–74.
[33] Y.A. Shin, S. Yin, X.Y. Li, S.B. Lee, S.M. Moon, J.W. Jeong, M. Kwon, S.J. Yoo, Y.M. Kim, T. Zhang, H.J. Gao, S.H. Oh, Nanotwin-governed toughening mechanism in hierarchically structured biological materials, Nat. Commun. 7 (2016) 10772.
[34] F.P. Yuan, X.L. Wu, Atomistic scale fracture behaviours in hierarchically nanotwinned metals, Philos. Mag. 93 (2013) 3248–3259.
[35] S. Zhang, J.Q. Zhou, L. Wang, Y. Wang, S.H. Dong, Effect of twin boundaries on nanovoid growth based on dislocation emission, Mater. Sci. Eng. A 582 (2013) 29–35.
[36] K. Lu, L. Lu, S. Suresh, Strengthening materials by engineering coherent internal boundaries at the nanoscale, Science 324 (2009) 349–352.
[37] L. Lu, Z.S. You, K. Lu, Work hardening of polycrystalline Cu with nanoscale twins, Scr. Mater. 66 (2012) 837–842.
[38] M.A. Meyers, A. Mishra, D.J. Benson, Mechanical properties of nanocrystalline materials, Prog. Mater. Sci. 51 (2006) 427–556.
[39] J.J. Xie, X.L. Wu, Y.S. Hong, Shear bands at the fatigue crack tip of nanocrystalline nickel, Scr. Mater. 57 (2007) 5–8.
[40] I. Gutierrez-Urrutia, F. Archie, D. Raabe, F.K. Yan, N.R. Tao, K. Lu, Plastic accommodation at homophase interfaces between nanotwinned and recrystallized grains in an austenitic duplex-microstructured steel, Sci. Technol. Adv. Mater. 17 (2016) 29–36.
[41] F.K. Yan, N.R. Tao, F. Archie, I. Gutierrez-Urrutia, D. Raabe, K. Lu, Deformation mechanisms in an austenitic single-phase duplex microstructured steel with nanotwinned grains, Acta Mater. 81 (2014) 487–500.
[42] F.K. Yan, N.R. Tao, K. Lu, Tensile ductility of nanotwinned austenitic grains in an austenitic steel, Scr. Mater. 84-85 (2014) 31–34.
[43] Q. Li, F.K. Yan, N.R. Tao, Enhanced fatigue damage resistance of nanotwinned austenitic grains in a nanotwinned stainless steel, Scr. Mater. 136 (2017) 59–63.
[44] Q. Li, F.K. Yan, N.R. Tao, D. Ponge, D. Raabe, K. Lu, Deformation compatibility between nanotwinned and recrystallized grains enhances resistance to interface cracking in cyclic loaded stainless steel, Acta Mater. 165 (2019) 87–98.
[45] S.S. Luo, Z.S. You, L. Lu, Thickness effect on fracture behavior of columnar–grained Cu with preferentially oriented nanoscale twins, J. Mater. Res. 32 (2017) 1–9.
[46] H.F. Zhou, H.J. Gao, A plastic deformation mechanism by necklace dislocations near crack-like defects in nanotwinned metals, J. Appl. Mech. 82 (2015) 671–675.
[47] J.A. Querin, J.A. Schneider, M.F. Horstemeyer, Analysis of micro void formation at grain boundary triple points in monotonically strained AA6022-T43 sheet metal, Mater. Sci. Eng. A. 463 (2007) 101–106.
[48] T.R. Bieler, A. Fallahi, B.C. Ng, D. Kumar, M.A. Crimp, B.A. Simkin, A. Zamiri, F. Pourboghrat, D.E. Mason, Fracture initiation/propagation parameters for duplex TiAl grain boundaries based on twinning, slip, crystal orientation, and boundary misorientation, Intermetallics 13 (2005) 979–984.
[49] R. Pippan, A. Hohenwarter, The importance of fracture toughness in ultrafine and nanocrystalline bulk materials, Mater. Res. Lett. 4 (2016) 127–136.
[50] A. Hohenwarter, R. Pippan, Anisotropic fracture behavior of ultrafine-grained iron, Mater. Sci. Eng. A 527 (2010) 2649–2656.
[51] A. Hohenwarter, R. Pippan, Fracture toughness evaluation of ultrafine-grained nickel, Scr. Mater. 64 (2011) 982–985.
[52] A. Hohenwarter, R. Pippan, Fracture of ECAP-deformed iron and the role of extrinsic toughening mechanisms, Acta Mater. 61 (2013) 2973–2983.

[53] P. Noell, J. Carroll, K. Hattar, B. Clark, B. Boyce, Do voids nucleate at grain boundaries during ductile rupture? Acta Mater. 137 (2017) 103–114.
[54] K. Jagannadham, H.G.F. Wilsdorf, Low energy dislocation structures associated with cracks in ductile fracture, Mater. Sci. Eng. A 81 (1986) 273–292.
[55] I.A. Ovid'ko, Review on the fracture processes in nanocrystalline materials, J. Mater. Sci. 42 (2007) 1694–1708.
[56] R. Pippan, The crack driving force for fatigue crack propagation, Eng. Fract. Mech. 44 (1993) 821–829.
[57] B. Cotterell, J.R. Rice, Slightly curved or kinked cracks, Int. J. Fract. 16 (1980) 155–169.
[58] Y. Lin, Q. Yu, J. Pan, F.H. Duan, R.O. Ritchie, Y. Li, On the impact toughness of gradient-structured metals, Acta Mater. 193 (2020) 125–137.
[59] G. Meneghetti, M. Ricotta, Evaluating the heat energy dissipated in a small volume surrounding the tip of a fatigue crack, Int. J. Fatigue 92 (2016) 605–615.
[60] A. Hohenwarter, R. Pippan, A comprehensive study on the damage tolerance of ultrafine-grained copper, Mater. Sci. Eng. A 540 (2012) 89–96.
[61] O. Kolednik, H.P. Stüwe, An extensive analysis of a JIC-test, Eng. Fract. Mech. 24 (1986) 277–290.
[62] K. Lu, F.K. Yan, H.T. Wang, N.R. Tao, Strengthening austenitic steels by using nanotwinned austenitic grains, Scr. Mater. 66 (2012) 878–883.
[63] H.T. Wang, N.R. Tao, K. Lu, Strengthening an austenitic Fe–Mn steel using nanotwinned austenitic grains, Acta Mater. 60 (2012) 4027–4040.
[64] X.H. Chen, J. Lu, L. Lu, K. Lu, Tensile properties of a nanocrystalline 316L austenitic stainless steel, Scr. Mater. 52 (2005) 1039–1044.
[65] T.L. Anderson, in: Fracture Mechanics: Fundamentals and Applications, third ed., CRC press, Boca Raton, 2017, pp. 301–303.